CENTRIFUGAL AND 3D EFFECTS ON THE NEAR TIP SECTION OF ROTATING BLADE

E. Berton, D. Favier, C. Maresca and M. Nsi Mba
L.A.B.M. Laboratory, USR 2164 of CNRS / University of Méditerranée
13288 Marseille Cedex 09, France

Abstract

The present paper concerns a new approach for determining local airloads on helicopter rotor blade sections in forward flight. The method is based on the momentum equation in which all the terms are expressed by means of the velocity field measured by a Laser Doppler Velocimetry technique. From a fundamental standpoint, the study emphasizes on the relative order of magnitude of all the terms involved in the momentum equation. In order to evaluate the finite span influence and the centrifugal effects on lift and drag, experiments are also carried out on 2D and 3D wings oscillating through dynamic stall conditions.

1 General Introduction

The understanding of rotary wings aerodynamics has been strongly developed during the past decades to improve their performance. The accurate prediction of spanwise airloads distribution and flowfield on helicopter rotor blades remains of primary importance for improving rotor aerodynamics performance, particularly the drag coefficient, conditioning the power requested from the engines for different flight capabilities (hover, forward, climb or descent). During the last decade, the development of numerical analysis and experimental methodologies have substantially improved the blade circulation distribution and the profile drag prediction, especially in hovering flight configurations [5], [6]. However, an equivalent contribution remains to be provided for forward flight configurations. Several experiments, performed in hover [7-9] have shown that the momentum equation and the Kutta-Joukovsky theorem have

made possible the estimate of the blade profile lift and drag including viscous effects, by only using the velocity field around and in the wake of the blade section. In this case, the methods, taking advantage of the axisymmetry of the flow in hover, can ignore the pressure distribution field and unsteady terms so that the equations of C_L and C_D only involve velocity distributions.

In the case of forward flight rotor configurations, the axisymmetry of the flow disappears giving rise to pressure terms contributions in the momentum equation. Nevertheless, it remains possible, as long as the incompressible case is concerned, to link the unsteady and pressure terms to local velocities via the unsteady Bernoulli's equation, introducing however the $\partial\varphi/\partial t$ term. This term, and more specifically the term $\partial(\varphi_\infty-\varphi_M)/\partial t$, can be estimated by the integral of the quantity $\vec{V}.\vec{d}$ along a streamline between M and infinity (M is a point of the control surface where the momentum equation is applied). In the first part of the paper, the experimental set up and velocity measurement technique implemented for the tests are described. Experiments are conducted in the S1-Luminy wind tunnel and provide a data base corresponding to velocities measured along a volume contour surrounding the blade at a given r/R. The second part of the present paper deals with the determination of airloads components deduced from the momentum equations applied to a volume contour suitable for forward flight conditions. It is shown that the different terms involved in the equations can be expressed in terms of local velocities by help of finite differences and Bernoulli's equation. In the third part of the paper, the different terms involved by the components of the aerodynamics force acting on

the blade at r/R=0.7 for $_b$= 90 deg and 270 deg, are compared for the advancing parameter µ=0.20. The drag and lift coefficients are deduced from the momentum equation. Such results are also compared to those obtained in the simplified case where volume terms and spanwise effects are neglected in the momentum equation. Moreover, in the last part of the paper airloads measured on retreating blades during dynamic stall, are compared to those obtained on a wing of same airfoil oscillating in pitch and fore-and-aft motion in 2D or 3D configuration. The evaluation of both finite span influence and centrifugal effects on dynamic stall are pointed out.

2 Aerodynamic forces deduced from the momentum equations
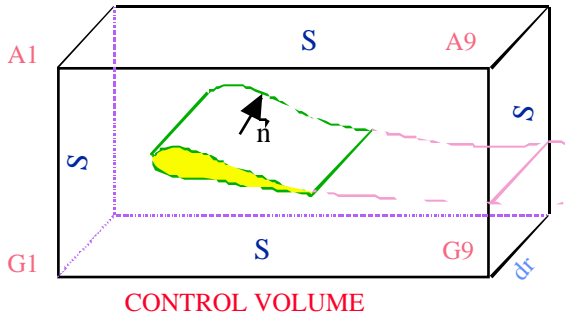

CONTROL VOLUME

Fig. 1 Control volume surrounding the blade section

When using the unsteady incompressible momentum equations applied to a control volume as defined in Fig. 1, the local forces acting on the blade section are given by :

$$\vec{F}=-\iiint_{v}\left[\frac{\partial \rho \vec{q}}{\partial t}+\vec{\Omega}\wedge\rho\vec{q}\right]dv-\iint_{S\infty}\rho\vec{q}.(\vec{q}d\ \vec{S})-$$
$$\underset{(I)}{} \underset{(II)}{} \underset{(III)}{}$$

$$\iint_{S\infty} p.\vec{n}d\ \vec{S}+\iint_{v}\rho\vec{g}dv \qquad (1)$$
$$\underset{(IV)}{} \underset{(V)}{}$$

2.1 Evaluation of the term (I) : $\iint_{V}\left[\frac{\partial \rho\vec{q}}{\partial t}\right]d\mathbf{V}$

The derivative of the velocity vector can be written through the following finite difference :

$\frac{\partial \vec{q}(t)}{\partial t}=\lim_{t\rightarrow 0}\frac{\vec{q}(t+\Delta t)-\vec{q}(t-\Delta t)}{2\Delta t}$ providing the approximated value of term (I) :

$$\iint_{V}\left[\frac{\partial \rho\vec{q}}{\partial t}\right]dv\approx\rho\sum_{i}\frac{\vec{qi}(t+\Delta t)-\vec{qi}\ (\ t\Delta t)}{2\Delta t}dvi \qquad (2)$$

The discretisation time step t is determined with respect to the accuracy of the velocity measurement. It is shown that the variation of velocities can be measured with a good accuracy when : $_b$=2 . t/T 5 deg (see Fig. 2).
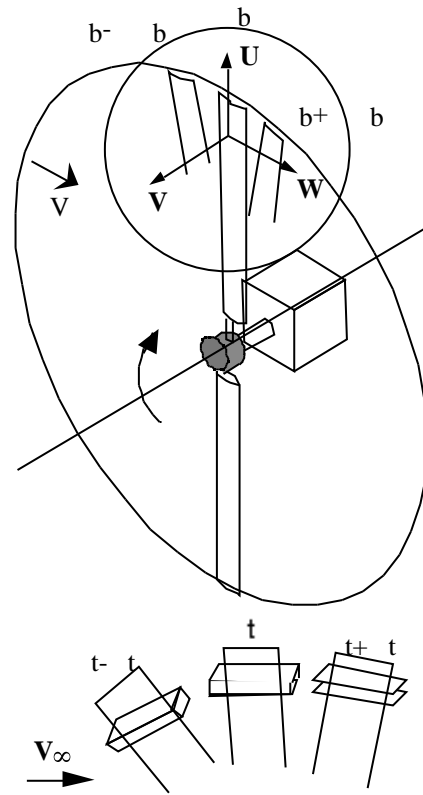

Fig. 2 Control volume at t, t+ t, t- t, around the blade azimuth $_b$

The external section bounding the volume V is discretised on its lateral part using the grid sketched in Fig. 3. The evaluation of the second term of equation (1) involves n elementary volumes, according to the grid defined in Fig. 3. The quantity $\vec{q}$ is considered for each elementary volume dv_i as the average value between the velocities measured at the center of the square (dz_ixdz_i), at r and r+ r.

2.2 Evaluation of the initial term (II) :

$$\iint_V (\vec{\Omega} \wedge \rho \vec{q}) dvi$$

In a fixed frame linked to the wind tunnel (see Fig. 2), the rotational $\bar{\ }$ and the velocity vector $\vec{q}$ are given by :
$$\vec{\Omega} = \begin{bmatrix} 0 \\ \Omega \cos\alpha s \\ \Omega \sin\alpha s \end{bmatrix} \qquad \vec{q} = \begin{bmatrix} U \\ V \\ W \end{bmatrix}$$

The rotational velocity W is constant, and a_s is defined as the rotor shaft angle. The evaluation of term (II) is obtained at time t by integrating the experimental values of $\bar{\ }$ $\vec{q}$ in the volume V.

2.3 Evaluation of the term (III) : $\iint_{S\infty} \rho\vec{q}.(\vec{q}.d\vec{S})$

The knowledge of experimental velocities in the mesh of the grid previously defined in Fig. 3 allows to numerically estimate the value of term (III).
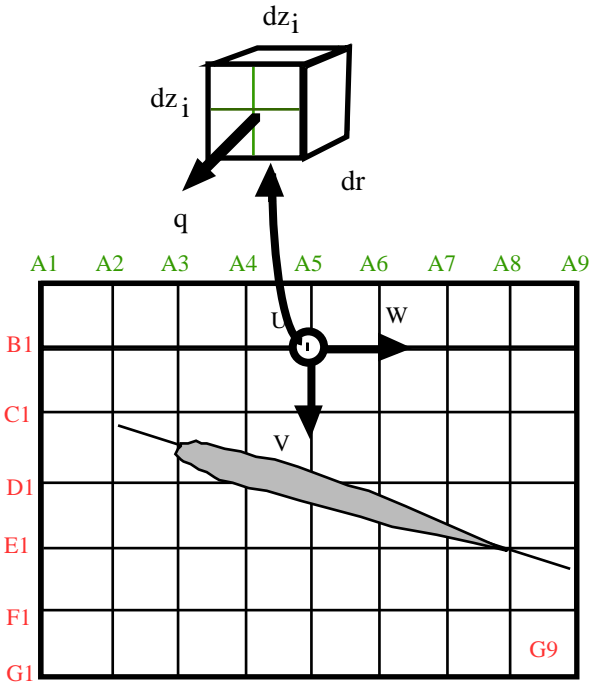

Fig. 3 Grid defining the lateral surface of V

2.4 Evaluation of the term (IV) : $\int_S p.\vec{n}d\vec{S}$

In order to avoid the measurement of the pressure field on the bounding surfaces, it is proposed to approximate the time dependent Bernoulli's equation by terms depending only on the velocity components. Particular attention is paid to the time-dependent term $\partial\varphi/\partial t$.

As shown in Fig. 4, if M' is assumed to be at the infinity, the Bernoulli's equation applied along the streamline MM' gives :
$$pM - p\infty = \frac{1}{2}\rho(q\infty^2 - qM^2) + \rho\frac{\partial(\varphi\infty - \varphi M)}{\partial t})$$

The integral (IV) concerning a closed surface can then be written as follows :
$$\int_S p.\vec{n}d\vec{S} = \int_S (p-p\ ).\vec{n}d\vec{S} = \int_S \frac{1}{2}\rho(q\ ^2 - q\infty) + \rho\frac{\partial(\varphi\ - \varphi)}{\partial t} .\vec{n}d\vec{S} \quad (3)$$

Along the streamline MM', if $\vec{V} = -\overrightarrow{grad}$ denotes the velocity vector in the grid plane, then : $\varphi M - \varphi\infty = \int_M^{M'} \vec{V}.d\vec{l} = \int_M^B Vdy + \int_B^N Wdz$, and the term $(\ - _M)/$ t can then be approximated by the finite difference equation :

$$\frac{\partial(\varphi\infty - \varphi M)}{\partial t} \approx \frac{\left(\sum_{MB} Vj\,dl\right)_{t+\Delta t} - \left(\sum_{MB} Vj\,dl\right)_t}{\Delta t} +$$
$$\frac{\left(\sum_{BN} Wi\,dl\right)_{t+\Delta t} - \left(\sum_{BN} Wi\,dl\right)_t}{\Delta t} \quad (4)$$

The above formulation shows that the term (IV) can be expressed only using the velocity measurements performed along the control contour. As far as air flows are concerned the gravity term (V) of equation (1) is neglected.
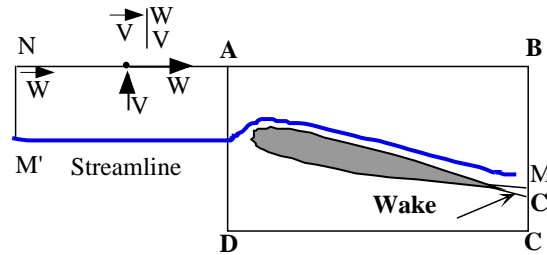

Fig. 4 Control volume for the pressure term determination

3 Experimental facilities and measurements procedure

The model-scale of a two bladed rotor is set up on the test rig installed in the S1-Luminy wind-tunnel test section, 3m in diameter, and 100ms^{-1} in maximum velocity (see Fig. 5). The test stand itself is mounted on an anti-vibration pad within the wind tunnel test hall. The rotor hub is mounted vertically by means of a supporting

mast. The model-rotor consists in a fully articuled rotor hub which can be equipped with interchangeable sets of blades.

For the purpose of the present study, the rotor system tested was a 2 bladed, 1.5 m diameter, with rectangular tip, OA209 airfoil blades, 0.05m in chord, rotating at a tip velocity $V_T=107$ ms^{-1}, in a wind speed of 21.4 ms^{-1}; the advancing parameter is µ=0.20. Several measurement techniques suited for surveying the flow in the near and far wake regions and around the blades have been developed (see [6-8]) including a long focal (2m to 2,5m) Laser Doppler Velocimetry (LDV) technique.
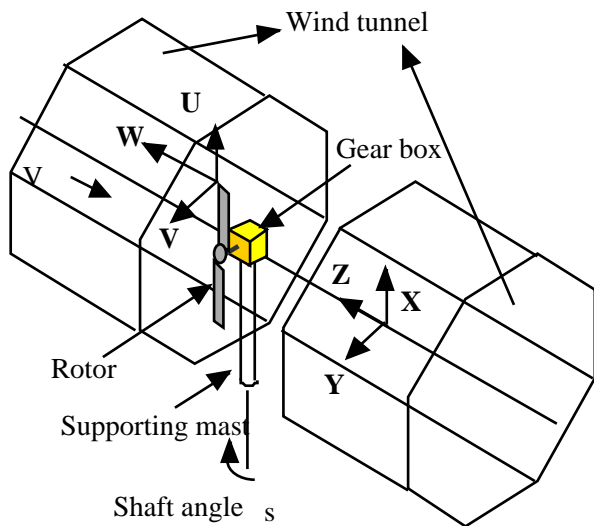
Fig. 5 S1-Luminy wind-tunnel experimental set-up

The three-dimensional velocity field around the blade is measured by a fiber optic laser velocimetry system performing two consecutive 2D measurements (see Fig. 6). In the vicinity of the blade the velocity components U,V and the axial component W are determined by LDV in a fixed coordinates system. A glycerin-based smoke generator was used to seed the flow and to produce particles of 1µm in diameter. The use of a 500 steps encoder provides an azimuthal resolution of 0.72 deg.

The velocity components are statistically averaged up to 200 samples per azimuthal step (=0.72 deg). Detailed characterization of the flowfield is made possible by a combination of

the 0.1 mm step resolution afforded by the laser optics traverse and the 0.2 mm diameter of the LDV system measuring volume. The initiation and synchronization of the instantaneous acquisition data are realized by means of a photo-cell delivering the azimuthal origin (= 0 deg) (see [7], [8]).
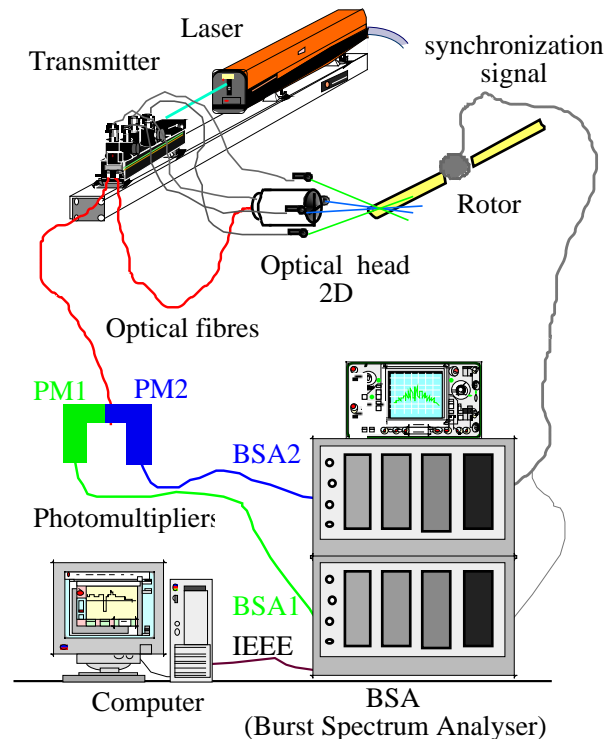
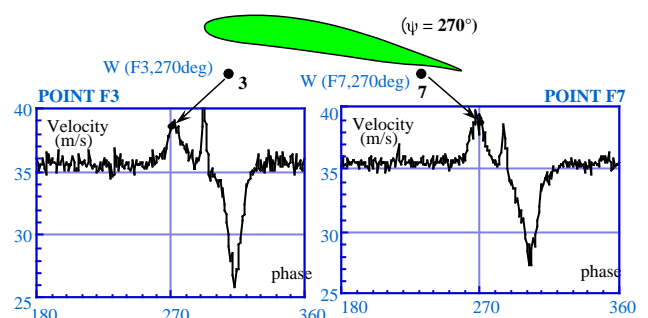**Fig. 6** Laser Doppler Velocimetry system.

Fig. 7 Example of velocity records

Fig. 7 shows the variations of the W component as a function of at points F3 and F7 of the grid previously defined in Fig. 3. The instantaneous values of W at these points for ${}_b=270$ deg (taken as an example) are given by the corresponding values on the graph at the phase 270 deg. The velocity components are so recorded at 63 points of the grid with an

accuracy less than 2% (see [7], [8]), for 3 azimuthal positions of the blade (ψ_b=270 deg, ψ_b- =265 deg, and ψ_b+ =275 deg) and 2 radial positions (r=0.70R, and r+ r=0.713R).

present study. These sources of error are first due to the instrumentation itself, the geometric alignment and positioning of the laser beams, the model geometry inaccuracies, ...

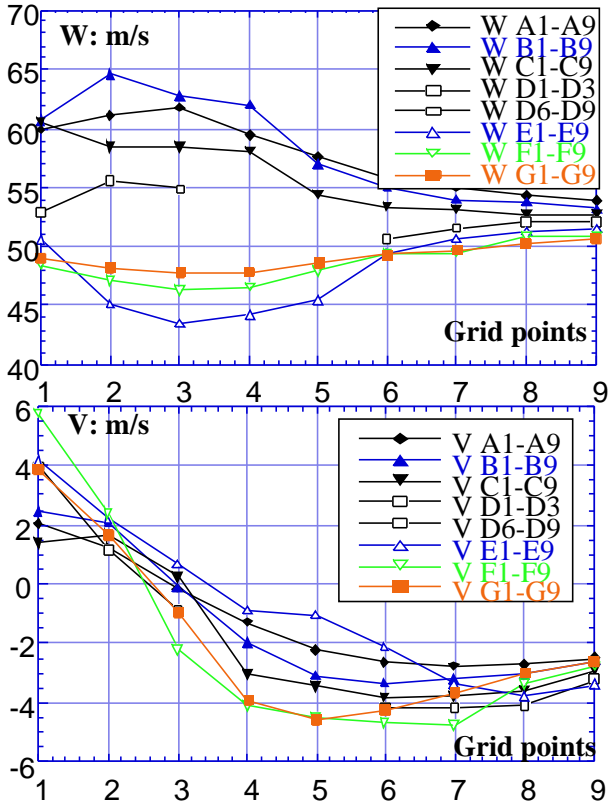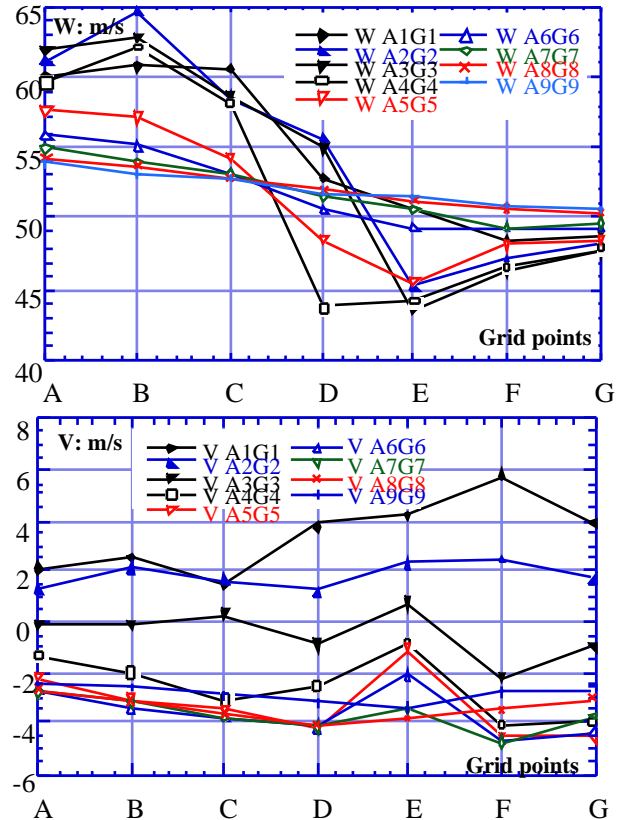**Fig. 8** V and W component variations along the grid lines at =270 deg.

Fig. 9 V and W component variations along the grid columns at =270 deg

Fig. 8 and Fig. 9 exemplify typical distributions of V and W obtained at =270 deg along lines and columns of the grid. The velocities are presented in a frame linked to the blade. It can be observed that the maximum values of W occur on the upperside as expected, and the maximum values of the induced vertical velocity occurs on the lower side. Concerning the U component (counted positively from the hub to the tip blade), Fig. 10 presents the plot of experimental results obtained around the airfoil along the grid columns.

4 Experimental uncertainty analysis

The measurement uncertainty analysis allows the separation and quantification of random and systematic errors in the different measurement methods implemented for the

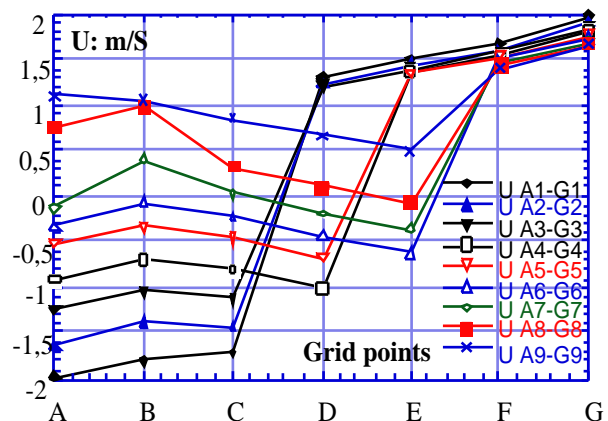**Fig. 10** U component variations along the grid columns at =270 deg

Moreover, the application of the momentum equations on the blade section, introduces additional inaccuracies because local

forces are obtained as a result of integrating the measured flow velocities. The estimation of all these experimental uncertainties has been performed [7], [8]. Specifically, concerning the Laser Doppler Velocimetry method, the procedure has been based on comparisons of measurements obtained from repeated runs and consists of a statistical estimate of variance of velocity measurements.

In the same way, the uncertainty in lift, drag and moment coefficients measurements on the OA209 airfoil has been estimated using the calibration data (the 3-components balance has been statically and dynamically calibrated). Measurement uncertainties, that quantify the deviations from averaged values, are summarized in Table 1.

Table 1 Uncertainty estimates

Measured Quantity	Uncertainty
Velocity field (Laser Doppler Velocimetry) Axial velocity W	±3%
Tangential and radial velocity V and U	±3% to 5 %
Local airloads on airfoil (3-components balance)	±1%
lift and drag coefficients (velocity integration)	±3 to 7%

5 Results and discussion

The aerodynamic force $\vec{F}=[X,Y,Z]$ given by equation (1), has been approximated in the case of the two-bladed rotor previously defined at the following conditions : $_b$ =90 deg and 270 deg, $=\pm$ 5 deg ; r/R=0.7, (r/R)=0.013 ; μ=0.2, with V_{wt}=21.4m/s (wind tunnel velocity) and R=107.1m/s ; $_s$=-12 deg, =10 deg and 14 deg. Using the experimental data obtained on the velocity vector at each point of the grid (defined in Fig. 3) at $_b$, $_b\pm$, and r/R+ (r/R), the integral involved in equation (1), can be calculated by help of discretized equations (2), (3) and(4).
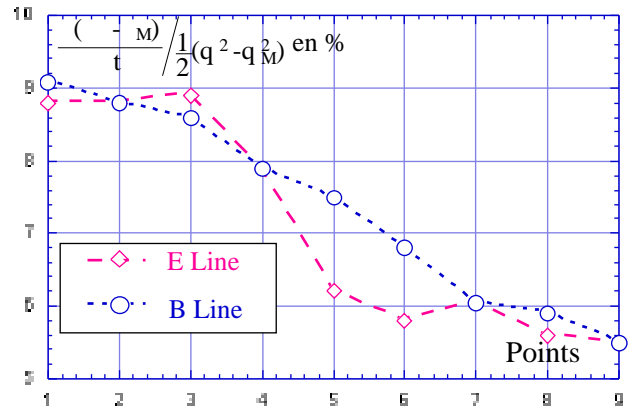

Fig. 11 Variations of the   ratio along the lines B and E at   = 270 deg

Concerning the term $\frac{\partial(\varphi\infty-\varphi M\,)}{\partial t}$ its evaluation by use of equation (4) in the grid has been compared to the term $1/2(V^2-V^2)$, where V is the velocity in the grid plane. It can be concluded from these comparisons that :

$$4.5\%\left(\frac{1}{2}\left(V\infty^2-V2\right)\right)\leq\frac{\partial(\varphi\infty-\varphi M\,)}{\partial t}\leq 9.3\%\left(\frac{1}{2}\left(V\infty^2-V2\right)\right)$$

As an example, Fig. 11 shows at $_b=270$ deg the variation of the η ratio defined as :

$$\eta=\left[\partial(\varphi\infty-\varphi M\,)\partial t\right]\Big/\left[\left(V\infty^2-VM^2\right)/2\right]$$ above and below the rotating plane (lines B and E).

5.1 Evaluation of the aerodynamic forces at θ=10deg, Ψ$_b$=270deg

The different values of all the terms I, II, III, and IV contributing to the components of the aerodynamic force by unit span length have been summarized in Table 2 for $_b=270$ deg. The percentage contribution   of each term to the total component of the force is also mentionned, pointing out that the main contribution to the aerodynamic forces are generated by terms III and IV, i.e transport of momentum and pressure effects. It may also be remarked that the value of the X component is mainly due to centrifugal effects appearing in term (IV) through the variation of W between r and r+ r.

Table 2 Components of force F at $\psi_b = 270$ deg

$\vec{F}$ Components	$X_{(N/m)}$	$Y_{(N/m)}$	$Z_{(N/m)}$
Term (I)	-0.121	-0.216	0.183
%	0.2	0.27	0.5
Term (II)	-0.39	0.005	-0.021
%	0.6	0.01	0.06
Term (III)	5.03	-28.81	-22.76
%	7.8	36.17	63.7
Term (IV)	-59.17	-50.62	12.71
%	91.4	63.55	35.74
$\vec{F}$ **FORCE** **F=-I-II-III-IV**	**54.65**	**79.45**	**9.89**

In the plane of the grid previously defined, the coefficients C_D and C_L at r/R=0.70 can be written by help of the components Y and Z of the areodynamic force F deduced from Table 2, and the induced incidence θ_i as defined in Fig. 12.

The induced incidence θ_i is given by the equation : $Arctan(\theta_i)= V_i/(V_{rot} - V_w)$, with : $V_w = -V_{wt} \cos\alpha_s$ where V_{wt} is the wind tunnel velocity and $V_{rot} = \Omega d \cos\beta + \Omega Ro$, β is the flapping angle, Ro the hub radius, and d the distance from the hub to the blade profile (Ro=0.11m, d=0.415m, and $\beta=-1.29$ deg at $\psi=270$ deg). V_i is the induced vertical velocity through the rotor experimentally measured in the present conditions as : V_i = -2.85m/s.

Lift L and drag D of the blade profile located at r/R, and the associated C_L and C_D, are given by the following equations:

$$L = Y\cos\theta_i + Z\sin\theta_i$$
$$D = Z\cos\theta_i - L\sin\theta_I$$

$$\begin{cases} CL = \dfrac{L}{1/2\rho V\infty^2 .c} \\ CD = \dfrac{D}{1/2\rho V\infty^2 .c} \end{cases}$$, where $V\infty$ is the intensity
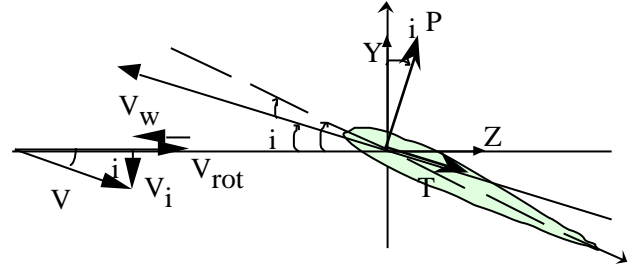
of the upstream velocity (see Fig. 14).

Fig. 12 Lift, drag, and induced angle of attack in the grid plane

The first line of Table 3 shows the results so obtained on lift, drag, C_L,C_D when using the 3D equation (1).

Table 3 Comparison between the different calculations of aerodynamic forces at $\psi_b = 270$ deg, $\theta=10$deg.

	$L_{(N/m)}$	$D_{(N/m)}$	C_L	C_D	C_L/C_D
3D : Equation (1)	79.85	5.74	0.871	0.063	13.82
2D : Equation (1) limited to terms (III) and (IV) with dU/dr=0	79.96	4.67	0.873	0.051	17.12
Kutta Law L= $\rho\Gamma V$	81.1		0.884		
2D POLAR			0.757	0.049	15.45

The analysis of the different terms involved in the equation (1) and presented in Table 2 clearly shows that some terms can be neglected as terms (I) and (II). Moreover, assuming that 3D effects remain light, i.e. the span variations and volume terms are neglected, the momentum equation can also be applied to the contour A1A9G1G9 defined on the grid, considering a 2D flow, and involving only the velocity vector values along the contour. Quantities X and Y so calculated provide new values of L and D as reported at the second line of Table 3. It can be observed that the lift is very well matched by the assumption of a 2D flow, while the drag is predicted at a value of 19% lower that the 3D case. The corresponding

values of C_L and C_D are also compared in the data of Table 3.

If assuming a 2D flow around the blade section, the lift can be related to the circulation by the equation of Kutta-Joukowsky: $L = \rho \Gamma V_\infty$, where the circulation can be determined experimentally from the distribution of the velocity along the contour A1A9G1G9 by :

$$\Gamma = \oint_{A1A9G9G1} \vec{u} \, \vec{l} \, .$$

The results shown at line 3 of Table 3 exhibit values slightly higher than in 3D or in simplified 2D configurations. However, it is worthy of note that the Kutta-Joukowski law can also be applied with success to a rotor blade profile, corresponding to the present experimental configuration.

The last line of Table 3 gives the C_L and C_D as obtained from the 2D polar of OA209 airfoil, at Reynolds number Re 5.10^5. Drag and lift coefficients are both found to be lower than in the case where the profile is in rotation.

It may be concluded from the analysis of the results in Table 3 that the effects of rotation tend to increase both the lift and drag coefficients of blade profiles resulting in a decrease of the profile aerodynamic efficiency C_D/C_L when compared to the 2D polar airfoil data, as shown from the last column of Table 3.

5.2 Evaluation of the aerodynamic forces at $\theta = 10deg$, $\Psi_b = 90deg$

The evaluation of the aerodynamic forces (L, D) by unit span length at the blade azimuth $\Psi_b = 90$ deg is summarized in Table 4 and Fig. 13 where the aerodynamic flowfield around the blade is plotted. With the assumption that the terms (I) and (II) can be neglected in equation (1), the momentum equation can be applied to the contour A1A9G1G9 defined on the grid in Fig. 13. As for the $\Psi_b = 270$ deg case, the calculated quantities X and Y, give values of L and D reported in Table 4. The Lift coefficient obtained by means of the momentum equation is compared with the value obtained through the equation of Kutta-Joukowsky.
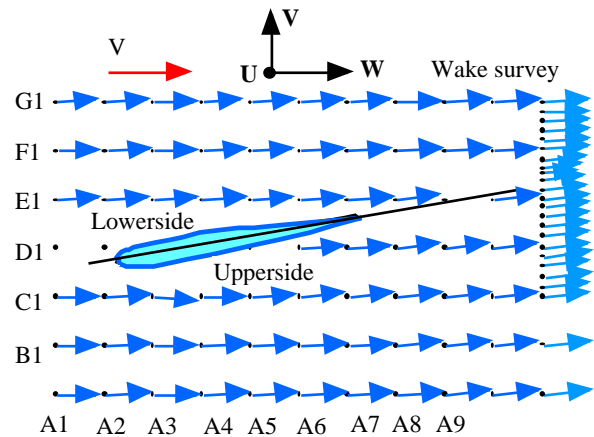

Fig. 13 Velocity in the measurement grid, r/R=0.7, =90deg

Table 4 Comparison between the different calculations of aerodynamic forces at $\Psi_b = 90$ deg, =10deg..

	L(N/m)	D(N/m)	CL	CD
Equation (1) limited to terms III and IV.	130.7	3.71	0.462	0.014
Kutta Law : L = V	109.35		0.456	

5.3 Evaluation of the aerodynamic forces at $\theta = 14deg$, $\Psi_b = 270deg$

It is important to check the method at higher pitch angle when the retreating blade was submitted to dynamic stall phenomenon. The Table 5 shows the results obtained on lift and drag when using the momentum equation limited to terms (III) and (IV) and the Kutta-Joukowski law, for the following parametric conditions : = 14deg, Ψ_b=270deg. The effective angle of attack calculated following the method described in paragraph 5.1 is about 12 deg.

Centrifugal and tip effects on dynamic stall can be characterized from comparisons with results obtained on a wing of same airfoil oscillating in a combined pitching fore-and-aft motion in 2D and 3D configurations. This motion implies the instantaneous variations of

velocity and incidence (V,) cycles selected from 3D aerodynamics rotor code results, which provide the stalling conditions encountered by the retreating blade sections (see [7], [8]).. It is shown from the code results that during the rotation the blade incidence at r/R=0.7 varies between 5deg and 15deg when μ=0.2 and =14deg.

Table 5 Comparison between the different calculations of aerodynamic forces at $_b$ = 270 deg, = 14 deg.

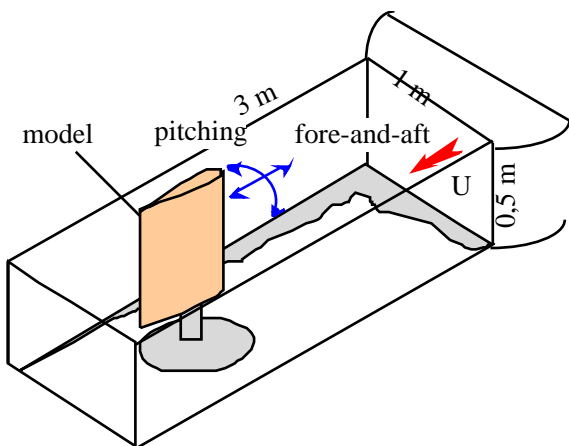|	L(N/m)	D(N/m)	CL	CD
Equation (1) limited to terms III, IV.	78.65	12.95	0.86	0.15
Kutta Law : L = V	76.88		0.84	
2D results on airfoil			0.97	0.22

Fig. 14 S2 Luminy wind-tunnel-Experimental set-up

The experimental investigation of the airfoil through dynamic stall conditions in a 2D/3D unsteady flow configuration has been performed in the S2-Luminy wind tunnel (Fig. 14). The aerodynamic response of the OA209 airfoil submitted to stall generated by simultaneous variations of velocity V and incidence , has been characterized. The experimental simulation is conducted here on a OA209 airfoil oscillating with same conditions of reduced amplitude and frequency (and k parameters) as those relative to the rotor blade sections in forward flight, presented above,

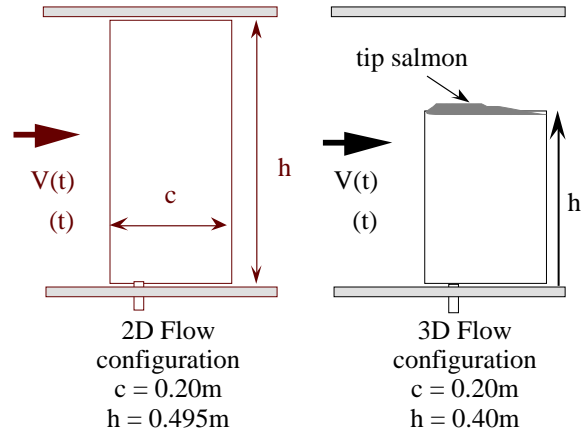resulting in the same variation of incidence and radius velocity.

Fig. 15 Schematics of 2D and 3D wings

In the 2D flow configuration, the tested airfoil consists in a rectangular wing of 0A209 airfoil (chord c = 0.2m; span h = 0.495 m) spanning the entire test section (see Fig. 15). In the 3D flow configuration the model consists in an half-wing of same 0A209 airfoil and chord (c = 0.2 m), with h = 0.40 m for span (see Fig. 15). On both models (2D or 3D), overall measurements of instantaneous lift, drag and moment coefficients are carried out by means of a 3-components balance statically and dynamically calibrated, embedded with the oscillating device.
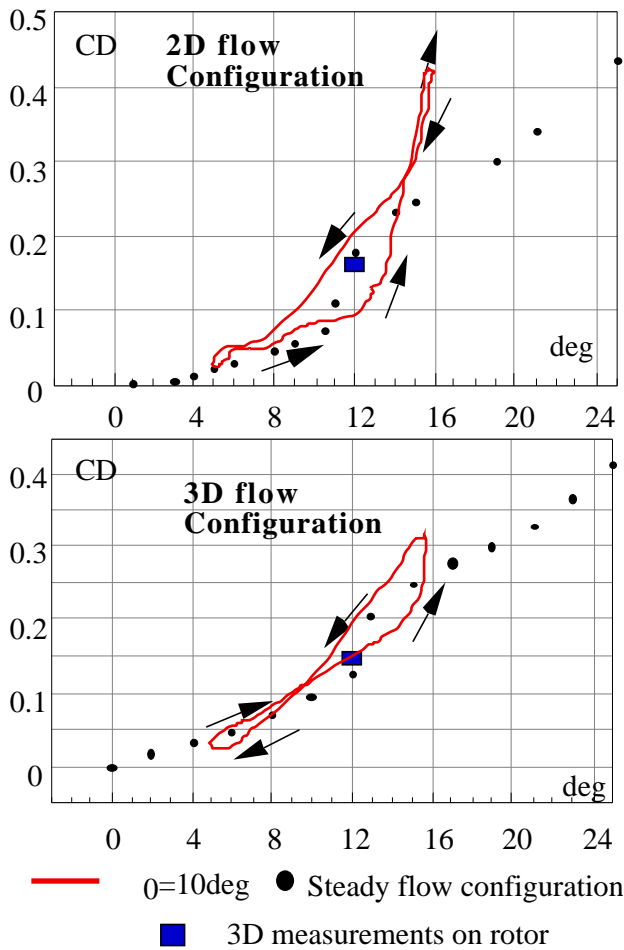
Fig. 16. Drag coefficient on airfoil in 2D and 3D flow configurations

Fig. 17. Lift coefficient on airfoil in 2D and 3D flow configurations

explained by the fact that tip effects counter balance centrifugal effects.

Fig. 16 and Fig. 17 give the variations of C_L and C_D measured in 2D and 3D flow configurations when the wing oscillates through dynamic stall between 5 deg and 15 deg corresponding to the variations of the angle of attack of the rotor blade in the test conditions of table 5. The hysteresis loops on C_L and C_D generated by the variations of incidence and velocity are well characterized. Results obtained on the rotor blade using the momentum equation are also shown in these Figures (squares). It can be noticed that the rotor blade results are close to the oscillating wing results and very close to the 2D configuration. Indeed, when the blade reaches the azimuth ψ_b=270deg, the effective incidence 12 deg is reached by decreasing values. Fig. 16 and Fig. 17 clearly show that 3D rotor results are closer to the decreasing branch of 2D oscillating airfoil results. This can be

6 Conclusions

The present paper has presented an experimental method to determine the force components acting on blade section of helicopter rotors in forward flight by only use of the velocity field determined by LDV. The relative magnitude of the different terms involved in the momentum and Bernoulli equations has been estimated. It has been shown that volume terms and spanwise effects can be neglected in the momentum equation, at least for the retreating blade azimuthal positions considered in the present forward flight configuration. Moreover, the Kutta-Joukowsky law has been applied to the rotating profile by integrating the velocity vector along a contour surrounding the blade profile. The resulting lift is in good agreement

with the one given by the momentum equation. Through dynamic stall conditions the lift and drag coefficients obtained on the rotating blade when using the momentum equation have been compared with those measured on an OA209 model oscillating in 2D and 3D flow conditions. It has been shown that dynamic stall on rotating blade induces C_L and C_D close to those obtained on 2D oscillating airfoils as already observed in (Bousman. 2001). It appears that tip effects counter balance centrifugal forces. The present work, involving a detailed experimental database has concerned two azimuth positions of the blade (90 deg and 270 deg). Results obtained, although encouraging, have to be duplicated in the future to other phases of rotation and other spanwise stations, in order to obtain the variation of the global forces and the profile drag acting on the blade at different azimuthal positions.

7 Acknowledgments

8 References

[1] Landgrebe, A.J. (1986). "Overview of Helicopter Wake and Airloads Technology", *Proceedings of 12th European Rotorcraft Foru*m, Paper n° 18, Garmish-Partenkirchen.

[2] Johnson, W. (1986). "Recent Developments in Rotary Wings Aerodynamics Theory", *A.I.A.A. Journal*, Vol. 24, n° 8, pp. 1219-1244.

[3] McCroskey, W.J. (1988). "Some Rotorcraft Applications of Computational Fluid Dynamics", *Basic Rotorcraft Research, Proceedings of 2nd International Conference*, pp. 1.1-1.25, Maryland.

[4] Chen, C.L. and McCroskey, W.J. (1988). "Numerical Simulation of Helicopter Multibladed Rotor Flow", *, Proceedings of 18th A.I.A.A. Aerospace Sciences Meeting*, A.I.A.A. Paper 88-0046, Reno.

[5] Maresca, C., Favier, D. and Nsi Mba, M. (1986). "A Prescribed Radial Circulation Distribution of a Hovering Rotor Blade", *Proceedings of 12th European Rotorcraft*, Paper n° 23, Garmish-Partenkirchen.

[6] Ramos, J., Nsi Mba, M., Berton, E., Favier, D. and Silva, M. (1994). "A Laser Velocimetric Investigation of the Airloads and Performance of a Model Helicopter Rotor in Hover", *, Proceedings of* the American Helicopter Society Aeromechanics Specialists Conference, Paper n° 8.1, San Francisco.

[7] Berton, E., Favier, D., Maresca, C. and Nsi Mba, M. (1994). "Airloads Determination on the Hovering Rotor Using a Laser Velocimetry Technique", AGARD, *, Proceedings of the 75th Fluid Dynamics Panel Meeting and Symposium on Aerodynamics and Aeroacoustics of rotorcraft*, AGARD CP N°. 552, Berlin.

[8] Berton, E., Favier, D., Maresca, C. and Nsi Mba, M. (1994). "A New Method of Laser Velocimetry for Airloads Determination on Hovering Rotor Blades" ICAS, *Proceedings of 19th Congress of Aeronautical Sciences*, ICAS Paper n °94-353, pp. 1610-1619, Anaheim.

[9] McAlister,K.W., Schuler, C.A., Branum, L., and Wu, J.C. (1995). "3-D Wake Measurement Near a Hovering Rotor for Determining Profile and induced Drag", *NASA Technical Paper 357*.

[10] Bousman, W.G. (2000). "Evaluation of airfoil dynamic stall characteristics for maneuverability", ERF, *Proceedings of 26th European Rotorcraft Forum*, pp. 38.1-38.21, The Hague.